The effect of powder preparation method on the artificial photosynthesis activities of neodymium doped titania powders

Hüsnü Arda Yurtsever [a,b,*,1], Muhsin Çiftçioğlu [a]

[a] Department of Chemical Engineering, Izmir Institute of Technology, 35430, Izmir, Turkey
[b] Department of Materials Engineering, Adana Science and Technology University, 01250, Adana, Turkey

ABSTRACT

The effects of nanostructure on the artificial photosynthesis activities of undoped and Nd doped titania (TiO_2) powders prepared by three different chemical co-precipitation methods were investigated. Substitutional/interstitial N and S doping was observed in powders due to the presence of high concentrations of HNO_3 (NP) and H_2SO_4 (SP) in the powder preparation media, respectively. Nd, N and S doping caused anatase/rutile phase transformation inhibition and crystallite size reduction in the nanostructure. Light absorption was significantly enhanced by Nd doping and the residual SO_4^{2-}/NO_x species in the nanostructure. Photocatalytic hydrogen production activity of Nd doped NP powder was 4 times greater than undoped NP powder at 700 °C and had a high purity ($CO:H_2$ ratio~0.00). CO was determined to be the main product in photocatalytic CO_2 reduction. NP powders had the highest CO yields and Nd doping enhanced CO production. The powders with high crystallite sizes and rutile weight fractions had the highest artificial photosynthesis activities.

© 2018 Hydrogen Energy Publications LLC. Published by Elsevier Ltd. All rights reserved.

Introduction

Research on the utilization of solar energy in order to compensate the increasing energy demand and to decrease the "Greenhouse Effect" gained significant interest in the last couple of decades. Artificial photosynthesis is being considered as a promising approach towards the synthesis of renewable, sustainable fuels like methane, methanol and hydrogen and the reduction of the global CO_2 content in the environment. The preparation and application of a very large number of photocatalytic materials were reported in artificial photosynthesis related research papers since the first pioneering studies conducted by Fujishima and Inoue [1,2].

Semiconductor materials are capable of triggering oxidation-reduction reactions taking place in artificial photosynthesis. Metal nanostructures (Ag, Cu), metal alloys (Cu-Ni), metal oxides (CeO_2, CuO_x), sulfides (CuS, CdS), nitrides (C_3N_4) [3] or metal organic frameworks (ZIF-8, MIL-125) [4] are highly photoactive materials that can be used in artificial photosynthesis. These materials are mostly hard to synthesize and expensive. Some of them have low chemical and thermal stability.

---

* Corresponding author. Department of Materials Engineering, Adana Science and Technology University, 01250, Adana, Turkey.
E-mail addresses: husnuarda@gmail.com, hayurtsever@adanabtu.edu.tr (H.A. Yurtsever), muhsinciftcioglu@iyte.edu.tr (M. Çiftçioğlu).
[1] Current affiliation: Department of Materials Engineering, Adana Science and Technology University, Adana, Turkey.

Titania (TiO_2) based materials are mostly preferred materials for artificial photosynthesis applications due to their superior chemical, optical and photocatalytic properties. Wide band gap of TiO_2 (anatase 3.2 eV, rutile 3.0 eV) is a drawback limiting the light absorption to only UV region representing 5% of the solar radiation. There are several methods for the enhancement of photocatalytic activity of TiO_2 such as doping [5—7], combining with low band gap materials [8—10], dye sensitization [11] or using different synthesis routes. Sol-gel, precipitation or hydrothermal methods are used to prepare highly active TiO_2 based photocatalysts [12—15]. Doped TiO_2 phases were synthesized with various methods for photocatalytic water splitting in many studies in the last 15 years. Comprehensive reviews were conducted by Ni et al. [16] and Oluwafunmilola and Mercedes [17] on photocatalytic hydrogen generation and CO_2 reduction including the mechanisms and TiO_2 modification methods to improve the artificial photosynthesis activity.

Research conducted in the last 10 years showed that rare earths, such as La, Nd, Eu, Sm, Yb, Pr and Ce doped TiO_2 powders showed higher activities than undoped TiO_2 powders due to their enhanced light absorption, higher surface areas and altered phase structures [18—28]. These studies were mostly on the environmental applications like photocatalytic degradation of dyes as probe molecules used for the simulation of polluted water.

Rare earth element incorporated titania phases were used in a few studies towards hydrogen production by water splitting [29—33] and CO_2 photoreduction related artificial photosynthesis [34—38]. Research on these materials has a vital importance towards improving the current state of understanding on artificial photosynthesis. Neodymium (Nd) among these rare earth elements has a variety of wide absorption bands in the visible light region which may enhance the light absorption properties of TiO_2 more effectively compared to other rare earth elements.

Photocatalyst preparation method parameters such as dopant type and doping level, heat treatment temperature and duration, the type of method used or photocatalytic reaction parameters such as reaction phase (gas or liquid), reaction medium type, catalyst loading, light source, reactor volume etc. were investigated in the given references dealing with artificial photosynthesis.

In the present work Nd doped TiO_2 powders were prepared by using three different chemical routes. The effects of powder preparation method and Nd doping on the nanostructure/electronic properties of TiO_2 powders were investigated. The photocatalytic activities of these powders in hydrogen production and CO_2 reduction were determined. The observed photocatalytic activities were related to the powder properties modified by the employed preparation method and Nd doping.

Materials and methods

Preparation of the powders

Undoped/doped TiO_2 photocatalysts were prepared by using 3 different chemical co-precipitation routes. The photocatalysts prepared by the dropwise addition of 1.6 M TTIP/ethanol solution to 0.65 M NH_4OH/ethanol solution were coded as AP. The other photocatalysts were prepared by dissolving hydrolyzed TTIP in 2.1 M H_2SO_4 or 3.3 M HNO_3 solutions. The final Ti^{4+} concentrations were 0.67 M and 0.61 M, respectively. These solutions were then added dropwise to an aqueous 1.2 M NH_4OH solution. The photocatalysts prepared by using H_2SO_4 and HNO_3 were coded as SP and NP, respectively. Powder precipitates were centrifuged and subsequently washed and dried at 70 °C overnight prior to heat treatment at 600 °C or 700 °C for 3 h.

Nd doped TiO_2 powders were prepared by following the same chemical routes. The only difference was the addition of predetermined amounts of neodymium nitrate (($Nd(NO_3)_3 \cdot 5H_2O$ Aldrich 99.9% trace metal basis) to TTIP containing solutions. Nd_2O_3 content was set constant at 0.1% (molar basis) in the final oxide powder. Photocatalyst preparation processes are schematically shown in Fig. 1. A commercial TiO_2 powder (Degussa Evonik P25) was also similarly characterized, further used in the artificial photosynthesis experiments and the results were given along with those of the powders prepared in this work.

Characterization of the powders

Phase characterization of the prepared powders was performed by Philips X'pert Pro XRD equipment with monochromated high-intensity ($\lambda = 1.54$ Å) CuKα radiation. The scanning rate was 2.5 2Θ/min between 5° and 80° with 0.033° step size. Characterization was conducted with 1—2 g of powder pressed in an aluminum cassette which was also used as reference material for the calculation of accurate peak positions. The crystallite sizes were calculated from the broadening of the (101) reflection for anatase and (110) reflection for rutile using Scherrer's equation [39]. The rutile and anatase weight fractions were determined by using the relation $x_A = (1 + 1.26 I_R/I_A)^{-1}$, where x_A is the anatase weight fraction, I_R and I_A are the intensities of the rutile (110) and anatase (101) peaks, respectively [40]. The determination of the anatase lattice constants for tetragonal geometry (a and c) was conducted by using expression $1/d^2 = (h^2 + k^2)/a^2 + l^2/c^2$, where d is the interplanar distance and hkl are the Miller (plane) indices. The lattice constants were determined by selecting two peaks (101 and 200 for anatase) [41]. Lattice strain was calculated by using Williamson-Hall (W-H) plot with at least 4 diffraction peaks to be used in the relation $\beta\cos\theta/\lambda = 1/\sigma + \eta\sin\theta/\lambda$, where σ is the effective particle size and η is the effective strain [41].

The existence and bonding states of the elements in the prepared powders were identified by using X-ray Photoelectron Spectroscopy (XPS) (XPSSPECS EA 300). Carbon C1s line at 284.8 eV was chosen as a reference for the correction of the peak positions [42]. The C1s, Ti2p, O1s, N1s and S2p spectra were fitted with a 70% Gaussian-30% Lorentzian product function peak shape model (GL30) in combination with a Shirley background by using XPS Peak Fit 4.1 software program. Quantitative analyses for the calculation of O:Ti and S:Ti atomic ratios were performed by using the corresponding peak areas and the atomic sensitivity factors of $Ti2p_{3/2}$, lattice O1s, and S2p as 1.2, 0.66 and 0.54, respectively [43].

UV—Vis diffuse reflectance spectra (DRS) of the prepared powders were recorded by Perkin Elmer Lambda 25 UV—Vis
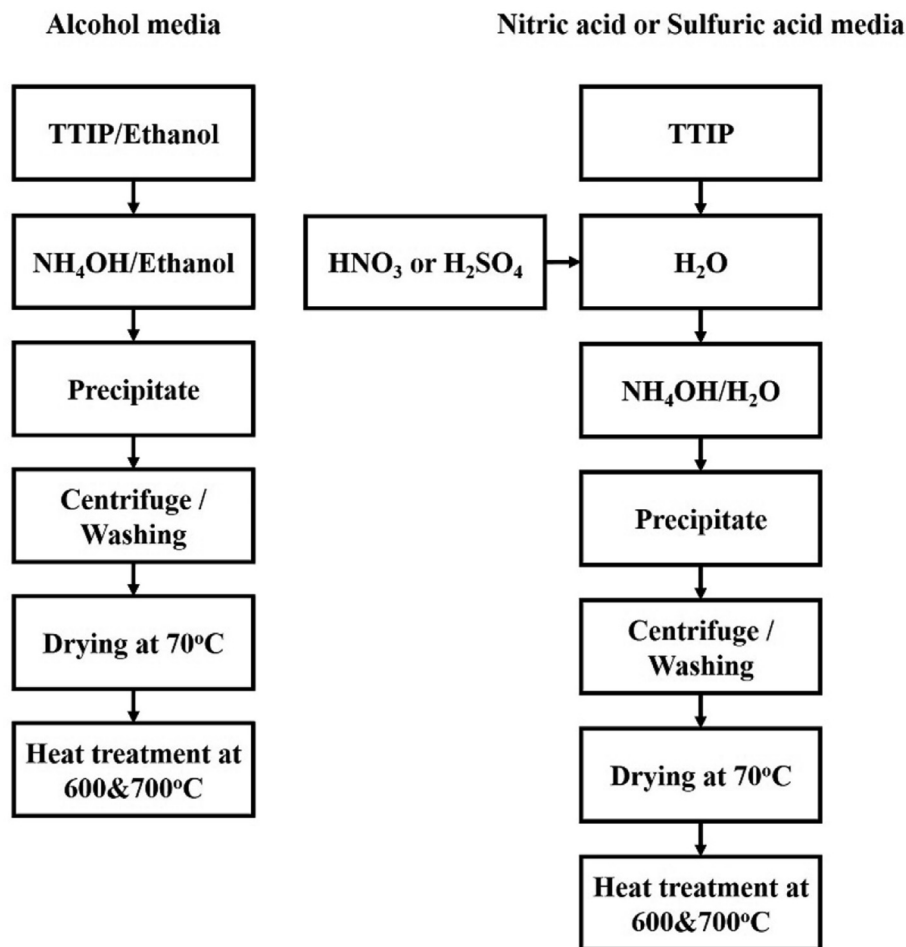
Alcohol media

Nitric acid or Sulfuric acid media

TTIP/Ethanol

↓

NH_4OH/Ethanol

↓

Precipitate

↓

Centrifuge / Washing

↓

Drying at 70°C

↓

Heat treatment at 600&700°C

TTIP

↓

HNO_3 or H_2SO_4 →

H_2O

↓

NH_4OH/H_2O

↓

Precipitate

↓

Centrifuge / Washing

↓

Drying at 70°C

↓

Heat treatment at 600&700°C

Fig. 1 − **Powder preparation process flow diagrams.**

Spectrophotometer equipped with an integrating sphere. Pellets 1.5 cm in diameter and 2−3 mm thickness were prepared by pressing the powders with a uniaxial press. $BaSO_4$ was used as the reference material. Band gaps of the prepared powders were determined by using Kubelka-Munk equation $F(R) = (1-R)^n/2 R$, where R is the reflectance, F(R) is Kubelka-Munk function and n = 2 or 0.5 for direct and indirect band gap, respectively [44].

Nitrogen adsorption and desorption isotherms and surface areas were obtained with Micromeritics Gemini V Surface Area Analyzer.

Photocatalytic water splitting and CO_2 reduction products (H_2, CO, CH_4) were identified and quantified by Agilent 7820A (Gas Chromatograph-GC) equipped with a Molecular Sieve 5A column and thermal conductivity detector (TCD). He (High purity, 99.99%) carrier gas volumetric flow rate was 20 mL/min. Inlet, oven and detector temperatures were 200 °C, 105 °C and 250 °C, respectively.

Photocatalytic water splitting and CO_2 reduction experimental setup

Photocatalytic hydrogen production experiments were performed simultaneously with in-situ copper (Cu) photodeposition. In this work Cu was chosen as cocatalyst instead

of platinum (Pt) because of its abundancy and cheapness compared to platinum.

In-situ Cu photodeposition was performed according to the following procedure. Stock solution of Cu^{2+} was first prepared by dissolving copper (II) nitrate ($Cu(NO_3)_2 \cdot 2.5H_2O$ Aldrich 99.9% trace metal basis) in deionized water at room temperature with a concentration of 1.5×10^{-4} g Cu/mL (2.4 mM Cu^{2+} ions). TiO_2 powders (0.15 g) were dispersed in water and the suspension was sonicated to disperse relatively weak agglomerates. Predetermined amounts of Cu stock solution and methanol (Merck, absolute) along with water were subsequently added to form the final mixture (100 mL, 25% v/v methanol-water) prior to UV−Vis irradiation (the output wavelengths of the lamp is between 300 nm and 2000 nm according to the spectrum provided by the supplier, OSRAM). Simultaneous hydrogen production was monitored and quantified by an online gas chromatograph (Agilent Technologies 7820A GC System) during in-situ Cu photodeposition process. A schematic illustration of Cu photodeposition mechanism is shown in Fig. 2.

A homemade Pyrex photoreactor was used in the photocatalytic water splitting and CO_2 reduction experiments and setup was constructed as shown in Fig. 3. The setup consists of mainly 3 parts:

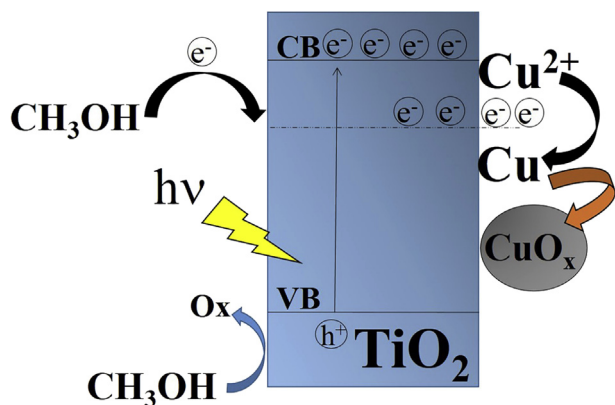• High purity (99.99%) CO_2 and N_2 (99.99%) source.

Fig. 2 – Schematic illustration of copper photodeposition mechanism.

- Homemade Pyrex glass photoreactor with N_2/CO_2 inlet and product gas outlet connected to online GC for water splitting experiments or sealed with a rubber septum for the sampling of gaseous products evolved in the photocatalytic CO_2 reduction experiments. Total volume of the reactor was 133 mL, liquid and gas volumes were 100 mL and 33 mL, respectively. Continuous agitation (at 1000 rpm) was supported by a magnetic bar and a stirrer during the photocatalytic activity tests to avoid mass transfer limitations and to hold the photocatalyst particles suspended.
- GC system for tracing artificial photosynthesis products.

Photocatalytic water splitting experiments were performed simultaneously with in-situ Cu photodeposition in continuous (by online GC quantification) operating mode. Photocatalyst powders (0.15 g) were dispersed in the reaction mixture containing 25% (by volume) methanol and predetermined amount of Cu^{2+} aqueous stock solution. N_2 was purged for 15 min prior to illumination in order to maintain anaerobe conditions in the photoreactor. Samples were withdrawn by the GC sampling valve (0.5 mL loop) every 10 min. Online calibration was conducted by a gaseous mixture containing H_2, CO and CH_4 (Refinery Gas Test Sample Agilent P/N 5080-8755). Online injections (four times) were performed by the sampling valve of the GC system.

Photocatalytic CO_2 reduction experiments were performed without in-situ Cu photodeposition in batch mode. Photocatalyst powders (0.1 g) were dispersed in 0.1 M NaOH which is used to enhance CO_2 solubility in water and act as hole scavenger. CO_2 was purged for 30 min prior to illumination to saturate the solution. The solution pH decreased from 12.6 to 6.9 at the end of CO_2 purge. Gas samples (volume: 1 mL) were withdrawn with predetermined time intervals and injected to GC system manually with a gas-tight syringe (Agilent, PN 5190-1535, 2.5 mL). The temperature inside the photoreactor was kept at ~45 °C by using a cooling fan and the pressure in the headspace was 1–1.1 bar during the experiments.

A calibration curve was constructed by using the refinery gas test sample for the quantification of CO evolved during the photocatalytic CO_2 reduction. CO was calibrated with two points (four repeats). Trace amounts of CH_4 and H_2 which evolved during the photocatalytic CO_2 reduction were not quantified.

Results and discussion

Characterization of the powders

XRD patterns of undoped/doped TiO_2 powders heat treated at 600 °C and 700 °C are given in Fig. 4. The characteristic diffraction peaks of anatase (JCPDS Card #841286) were identified in the XRD patterns of all the prepared powders. Anatase phase was found to be the only phase for undoped SP powder
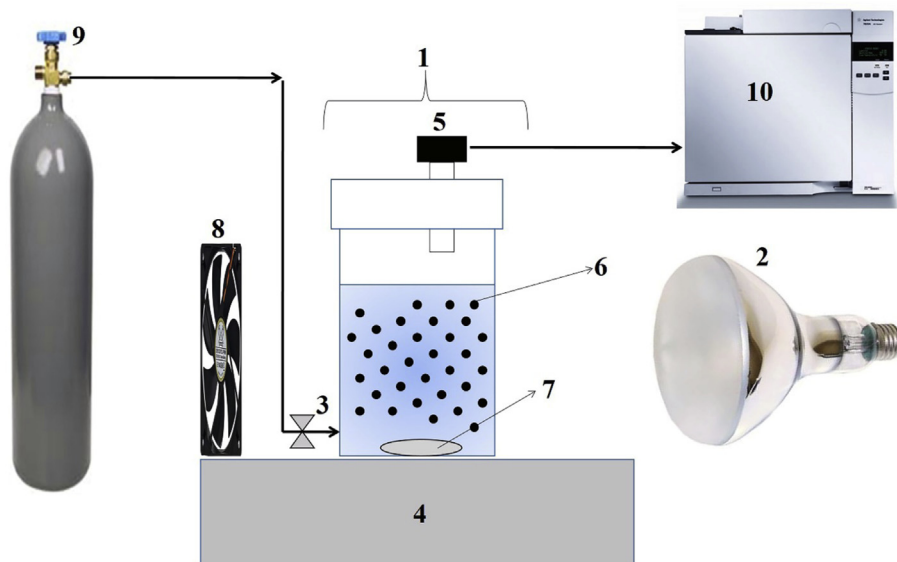

Fig. 3 – Photocatalytic water splitting/CO_2 reduction setup. 1: Photoreactor, 2: UV–Vis lamp (Osram Ultravitalux 300 W), 3: N_2/CO_2 inlet, 4: Magnetic stirrer, 5: Gas outlet, 6: Photocatalyst particles, 7: Magnetic bar, 8: Cooling fan, 9: N_2 or CO_2 source, 10: Gas Chromatograph.
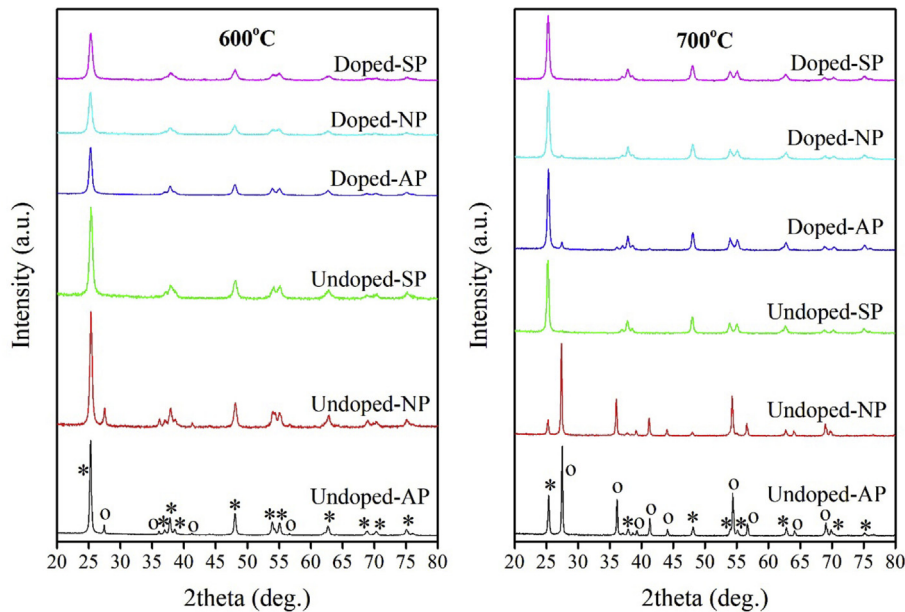
Fig. 4 – XRD patterns of undoped/doped TiO$_2$ powders heat treated at 600 °C and 700 °C.

while it coexists with the rutile phase (JCPDS Card #870920) in the undoped powders of AP and NP heat treated at 600 °C. Anatase was the only phase for the doped powders heat treated at this temperature. The nanophase structure of the undoped powders heat treated at 700 °C was dominated by rutile phase with an exception of SP powder. The main phase in the doped powders heat treated at this temperature was found to be anatase. The phase structure and physical properties such as crystallite size, rutile weight fraction, lattice constants, lattice strain and BET surface area (S$_{BET}$) of the prepared powders are summarized in Table 1.

Anatase phase is known to be more active than rutile phase in photocatalytic processes and rutile phase has a lower band gap than anatase phase which makes rutile phase to utilize solar light more efficiently than anatase phase. These two reasons promoted scientists to prepare TiO$_2$ powders having a mixture of anatase and rutile phases in the nanostructure. Crystallinity is also an important parameter in photocatalytic applications. An optimized crystalline structure may provide

a high photocatalytic activity. Well-developed crystalline structures with high specific surface areas can be obtained by keeping the heat treatment temperature at an optimum level, not too low in order to have well-developed crystalline structure and not too high in order not to decrease the surface area. It was, therefore, intended in this work to prepare various undoped/doped TiO$_2$ powders with anatase rich and well developed crystalline nanostructure which were evidenced by the crystallite sizes and rutile weight percentages given in Table 1.

Anatase crystallite sizes were determined to be in the 34.1–17.8 nm range for the undoped powders heat treated at 600 °C which was significantly reduced (19.2–16.2 nm range) with Nd doping. The crystallite sizes increased with the heat treatment temperature for both undoped and doped powders. Rutile weight fraction was found to be the highest for the undoped NP powders heat treated at 600 and 700 °C.

Anatase lattice constant c changed significantly with the preparation method and Nd doping. The lattice constant c

Table 1 – Properties of undoped/doped TiO$_2$ powders heat treated at 600 °C and 700 °C.

Photocatalyst	Anatase crystallite size (nm)	Rutile wt. frac. (%)	Anatase lattice parameters		Anatase lattice strain (%)	S$_{BET}$ (m^2/g)	Zeta potential (mV)
			a (Å)	c (Å)			
Undoped-AP-600	34.1	10.0	3.77	9.39	0.56	27.3	−31.0 (±4.1)
Undoped-NP-600	22.6	15.9	3.77	9.35	0.48	54.5	−29.1 (±4.9)
Undoped-SP-600	17.8	0	3.78	9.31	0.78	84.5	−35.0 (±1.2)
Doped-AP-600	19.2	0	3.78	9.41	0.77	47.7	−37.3 (±9.0)
Doped-NP-600	16.3	0	3.78	9.33	0.68	88.4	−35.5 (±5.5)
Doped-SP-600	16.2	0	3.77	9.26	1.17	83.2	−26.5 (±3.9)
Undoped-AP-700	40.8	74.7	3.77	9.42	−0.54	15.8	−35.5 (±2.1)
Undoped-NP-700	37.2	89.0	3.77	9.47	N/A	14.2	−35.5 (±2.5)
Undoped-SP-700	27.9	1.2	3.77	9.39	0.59	50.2	−28.6 (±2.6)
Doped-AP-700	27.4	9.3	3.77	9.39	0.65	33.8	−31.8 (±5.0)
Doped-NP-700	23.1	3.8	3.77	9.37	0.34	55.5	−29.8 (±3.4)
Doped-SP-700	22.3	Trace	3.77	9.38	0.19	57.7	−35.0 (±2.8)

values were calculated to be the lowest for SP powders. Nd doping caused a significant decrease in the lattice constant c which may be attributed to the decrease in the crystallite size as was previously stated in the literature [45] or the presence of oxygen vacancies in the nanostructure which may be due to a possible segregation of Nd oxides/hydroxides on the grain boundaries or interstitial accommodation of Nd^{3+} ions in the TiO_2 lattice. It may be difficult for Nd^{3+} ions to replace the Ti^{4+} ions in the lattice since the ionic radius of Nd^{3+} (112.3 p.m.) is significantly higher than that of Ti^{4+} (68 p.m.).

The lower c values obtained with NP and SP powders may be attributed to the significantly lower crystallite sizes compared to AP powders and to the formation of oxygen vacancies which may be created by the substitutional incorporation of N or S atoms for O and Ti atoms in the TiO_2 lattice. Substitutional incorporation may be possible since high concentrations of HNO_3 or H_2SO_4 were used during the synthesis of these powders. Nitrogen ions most likely substituted lattice oxygen forming N-Ti-N bond and formed a mixed N2p state with O2p state above the valence band [46]. Substitution of S with O is difficult since S^{2-} ion (170 p.m.) is relatively larger than O^{2-} ion (126 p.m.) compared to N^{3-} ion (132 p.m.). More energy is required for the formation of Ti-S bond instead of Ti-O bond; however XPS analysis revealed that Ti2p3/2 binding energy of SP powder was higher than the other powders heat treated at 600 °C which may be interpreted as Ti-S bonds were formed in the SP powders. The level of S substitution may be at a very low level since S^{2-} peak was not detected in the XPS spectra of the SP powders. The substitution of Ti^{4+} (68 p.m.) with S^{4+} (37 p.m.) or S^{6+} (29 p.m.) is more favourable [47] as will be later discussed in our XPS results given in Fig. 6.

The lattice strains were determined to be the highest for SP and the lowest for NP (except for the doped powders at 700 °C). Lattice strain did not show a direct correlation with the crystallite size and showed variation depending on the phase composition. A negative slope in the W-H plot indicates the presence of compressive strain, while a positive slope indicates the presence of tensile strain [48]. All the prepared powders showed tensile strain; the variations are significant and can be related to the significant variation in the crystallite sizes and phase compositions. Highest tensile strain was calculated for the SP powders which have smaller crystallite sizes and a nanophase structure dominated by anatase phase. NP powders which have relatively smaller crystallite sizes and higher rutile phase content, showed lower strain compared to AP and SP powders.

It is well known that strain can be reduced by increasing the heat treatment temperature for ceramic materials. Excess number of disordered atoms and defects on the grain boundaries are present in the microstructure of the powders heat treated at low temperatures. These atoms and defects cause a stress field (surface strain). Increase in the heat treatment temperature causes some structural changes such as grain growth and phase transformation. The level of disorder and the number of defects decrease at higher temperatures. XRD pattern of NP powders indicated that anatase to rutile phase transformation occurs at a lower temperature and the structure stabilizes earlier with the formation of a less defective structure compared to the other powders.

Surface areas of the prepared powders were determined to be in the following order: SP > NP > AP. Powders with higher surface areas may be prepared by precipitation method compared to sol-gel method. The reason for obtaining higher surface areas with SP powders may be attributed to the presence of SO_4^{2-} ions in the nanostructure inhibiting the anatase to rutile phase transformation [49].

In general the change in the nanophase structure were similar for the undoped and doped powders heat treated at 600 °C, however at 700 °C, SO_4^{2-} or NO_x ions were significantly removed from the nanostructure due the increased heat treatment temperature. As a result the effect of these ions on the nanophase evolution was minimized by increasing the heat treatment temperature.

UV–Vis DRS spectra and estimated band gap energies of the prepared powders are given in Fig. 5 and Table 2, respectively. DRS spectra of NP and SP indicated absorption in the blue and green light region for undoped/doped powders heat treated at 600 °C. N or S doping of TiO_2 matrix may have created energy levels slightly above the valence band edge of TiO_2. This phenomenon increased the light absorption range of NP and SP powders. Visible light absorption may also be attributed to a typical absorption feature of N and S doped TiO_2 based materials arising from the electron transfer from surface states of NO_x [50] or SO_4^{2-} species to the conduction band of TiO_2 [51]. The estimated band gap energies given in Table 2 indicated that NP and SP powders can utilize the visible light photons. The spectra of Nd doped powders showed blue shift (shift to lower wavelengths), however a blue-shift in the band gap energy does not always signify a decrease in the visible light absorption, since there are several absorption bands in the visible light region for Nd doped powders. The large absorption bands at the wavelengths of 515, 529, 588, 684, 747 nm are the characteristics absorption bands of Nd^{3+} ion resulting from 4f-4f transitions.

Ti2p, O1s, S2p and N1s XPS spectra of the powders are given in Fig. 6. Ti2p core level spectra contain two main peaks of $Ti2p_{1/2}$ and $Ti2p_{3/2}$. The $Ti2p_{1/2}$ and $Ti2p_{3/2}$ spin-orbital splitting photoelectrons for all powders are located at binding energies of ~465.2 eV and ~459.3 eV, respectively. The difference between these two peaks is about 5.9 eV which showed that prepared undoped and doped TiO_2 powders mostly consist of Ti^{4+} oxidation state with small contribution of Ti^{3+} which may be formed due to oxygen deficiencies in the TiO_2 lattice. O1s peak appearing at 529 eV is attributed to the signal of oxygen in the TiO_2 lattice. Shoulder appearing at 531.5 eV is the signal of Ti-OH or C-OH. S2p peak position at 169 eV was attributed to S^{6+}. This peak may be assigned to the presence of SO_4^{2-} ions originating from H_2SO_4. The intensity of this peak increased with Nd doping and decreased with increasing heat treatment temperature which may indicate that Nd doping may increase the binding of Ti with S and sulfated TiO_2 may be easily prepared by using Nd as the dopant. The decrease in the intensity of this peak at 700 °C may be attributed to SO_4^{2-} ions' leaving the nanostructure. Substitution of sulfur and oxygen atoms which has the indication of S^{2-} binding energy peak at 163 eV [52] might have occurred at low levels since that peak was not detected in the XPS spectra of SP powders. The present SO_4^{2-} ions may mostly locate on the grain boundaries restraining the growth of
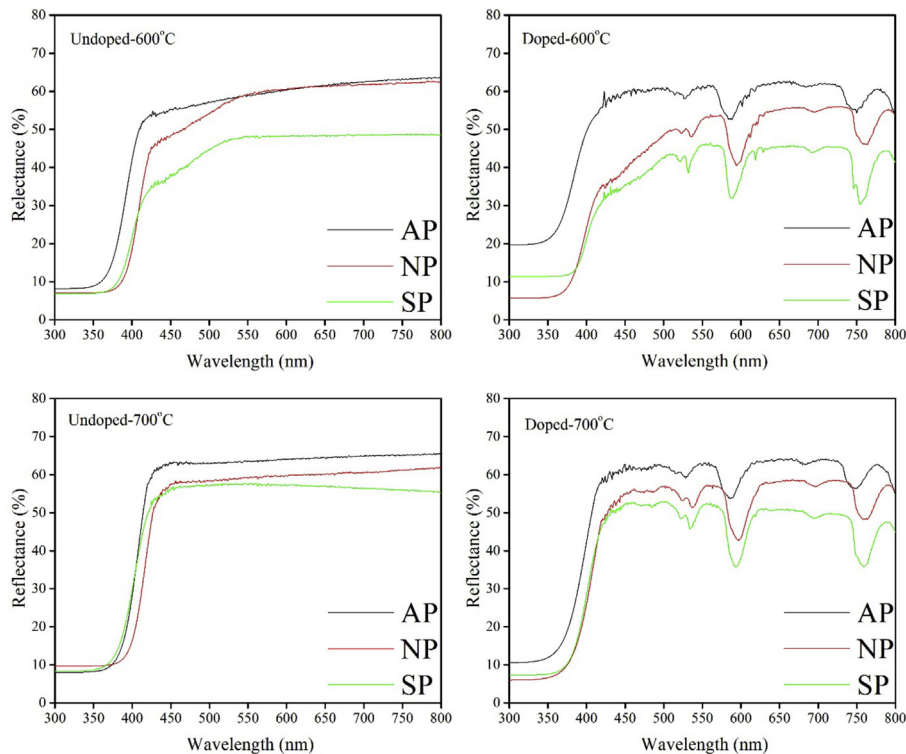
Fig. 5 – UV–Vis DRS spectra of undoped/doped TiO_2 powders heat treated at 600 °C and 700 °C.

anatase crystallites. N1s spectra of the NP powders indicated that molecularly chemisorbed and interstitial N atoms may be present in the nanostructure of these powders according to the presence of the relatively small peak at ~400 eV [53] in the XPS spectra of NP powders. The peak appearing around 396–397.5 eV was attributed to the formation of Ti-N bond for the undoped NP powder heat treated at 700 °C indicating a possible N substitution in the TiO_2 lattice which was absent in the other powders.

Binding energies of $Ti2p_{3/2}$ of undoped and doped TiO_2 powders heat treated at 600 °C and 700 °C are given in Fig. 7. SP powders heat treated at 600 °C possessed higher binding energies due to a possible Ti-S bonding. Substitution of S with O is difficult since S^{2-} ion (170 p.m.) is relatively larger than O^{2-} ion (126 p.m.) compared to N^{3-} ion (132 p.m.). More energy is

required for the formation of Ti-S bond instead of Ti-O bond. XPS analysis revealed that $Ti2p_{3/2}$ binding energy of SP powders heat treated at 600 °C were higher than the other powders which may be interpreted as Ti-S bonds were formed in the SP powders. The level of S substitution may be at a very low level since S^{2-} peak was not detected in the XPS spectra of the SP powders. The substitution of Ti^{4+} (68 p.m.) with S^{4+} (37 p.m.) or S^{6+} (29 p.m.) is more favourable [47] which was also confirmed by our XPS results. The lower binding energies of NP and SP powders heat treated at 700 °C indicated the presence of a more oxygen defective structure for NP and SP compared to AP powders which may be due to the presence of substitutional N or S atoms in the TiO_2 lattice. Nd doping caused a decrease in the $Ti2p_{3/2}$ binding energies which may be due to the presence of increased oxygen defects compared to the undoped TiO_2 powders. Electronic properties such as O:Ti and S:Ti ratios derived from XPS spectra and band gap energies estimated from UV–Vis DRS spectra of the powders are given in Table 2. The results indicated that most of the powders are oxygen deficient according to O:Ti ratios and the level of deficiency was increased with Nd doping at 700 °C. The calculated S:Ti ratios indicated that the level of S content increased with Nd doping for both heat treatment temperatures which may due to the affinity of rare earth ions to sulfate ion. The table also indicated that S content decreased with increasing heat treatment temperature.

Photocatalytic activities of the powders

Photocatalytic water splitting
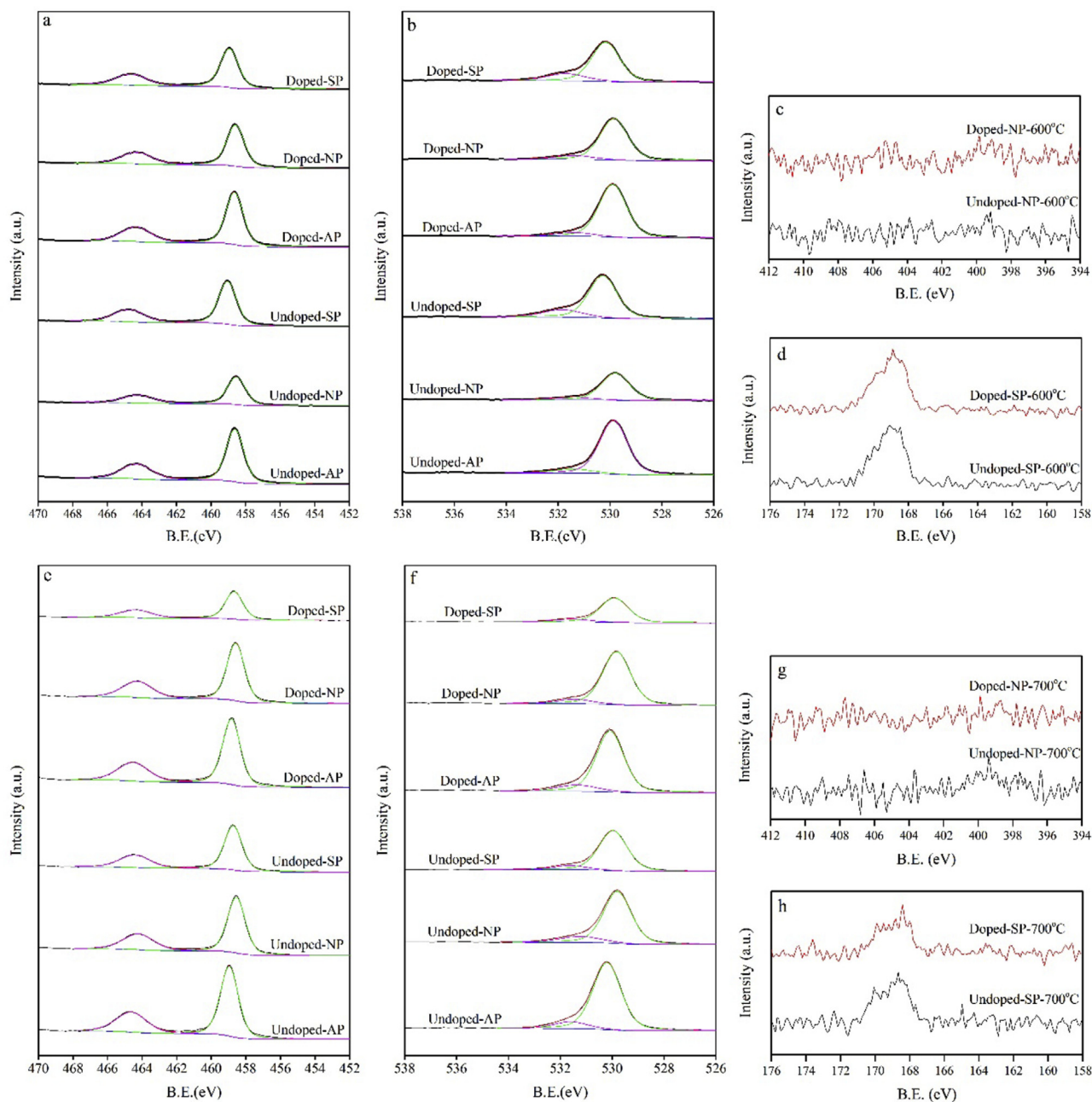Time dependent hydrogen production, hydrogen yields per uint surface area of the photocatalyst and CO/H_2 ratios

Table 2 – Electronic properties of the powders.

Photocatalyst	O:Ti ratio	S:Ti ratio	Direct/Indirect band gap energy (eV)
Undoped-AP-600	1.93	—	3.26/3.05
Undoped-NP-600	1.83	—	3.10/2.93
Undoped-SP-600	1.88	0.070	3.15/2.93
Doped-AP-600	1.91	—	3.24/2.93
Doped-NP-600	1.88	—	3.19/2.94
Doped-SP-600	1.88	0.072	3.08/2.83
Undoped-AP-700	2.02	—	3.15/2.94
Undoped-NP-700	1.94	—	3.04/2.86
Undoped-SP-700	1.92	0.029	3.17/2.92
Doped-AP-700	1.92	—	3.23/2.93
Doped-NP-700	1.97	—	3.19/2.90
Doped-SP-700	1.88	0.032	3.17/2.94
Degussa	1.86	—	3.14/2.94

Fig. 6 — XPS spectra of undoped/doped TiO_2 powders: (a) Ti2p, (b) O1s, (c) N1s, (d) S2p, heat treatment temperature: 600 °C and (e) Ti2p, (f) O1s, (g) N1s, (h) S2p, heat treatment temperature: 700 °C.

obtained at the end of 120 min with undoped/doped TiO_2 powders heat treated at 600 °C and 700 °C are given in Figs. 8 and 9, respectively. Hydrogen production rates are low for all the powders at the very beginning of photocatalytic water splitting, since in situ Cu photodeposition takes place during this period. Hydrogen develops in the head space of the photoreactor and continues to evolve linearly after a certain time.

The highest hydrogen yields were obtained with NP powders for the heat treatment temperature of 600 °C. Nd doping increased the hydrogen yields of AP powders at this temperature. The highest hydrogen yields were obtained with undoped SP powder and doped NP powder for the heat

treatment temperature of 700 °C which increased with Nd doping for NP powder. Hydrogen production per unit surface area of the photocatalyst were mostly the highest for NP powders which may indicate that these powders have highly active surfaces towards photocatalytic water splitting compared to the other powders. The surface reactivity decreased with Nd doping at 600 °C for NP and SP powders whereas it increased for the AP powder. The surface reactivity was highly affected by the heat treatment temperature. The surface reactivity of Nd doped powders increased at 700 °C. At this temperature Nd doping caused a decrease in the hydrogen production per unit area for AP and SP powders
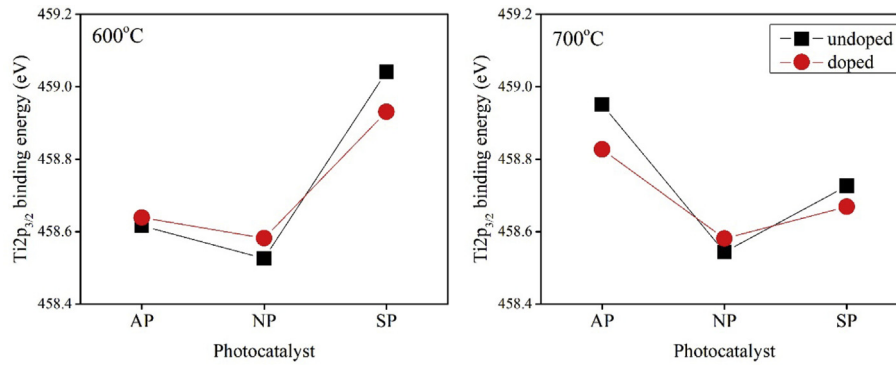
Fig. 7 – Binding energies of Ti2p$_{3/2}$ of undoped/doped TiO$_2$ powders heat treated at 600 °C and 700 °C.
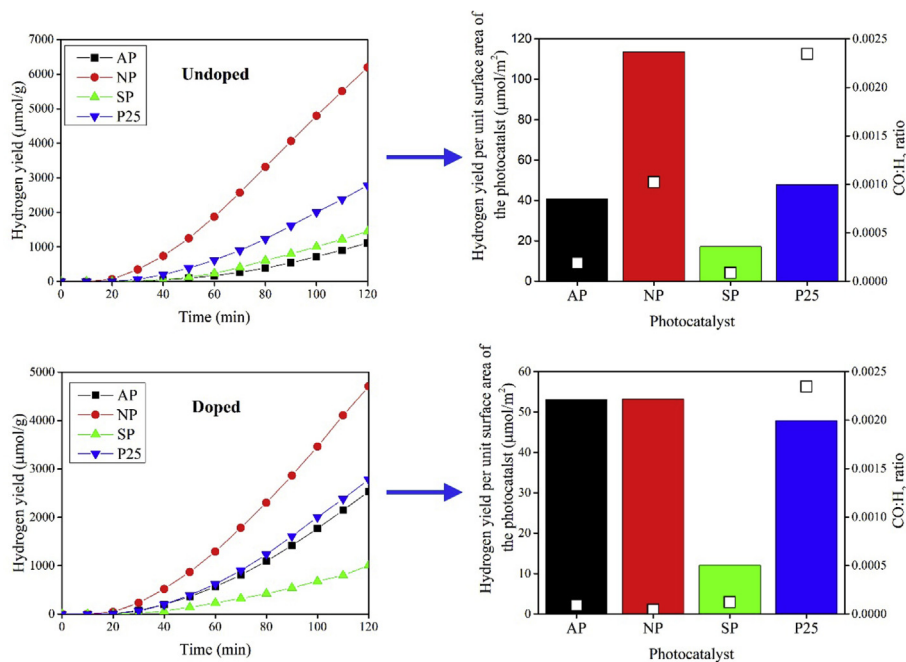

Fig. 8 – Time dependent hydrogen production (the left figure), hydrogen yields per unit surface area of the photocatalyst and CO:H$_2$ (□) ratios obtained at the end of 120 min (the right figure) with undoped/doped photocatalysts heat treated at 600 °C.

while the surface reactivity of NP powder increased with Nd doping. The lowest CO/H$_2$ ratios were obtained with the doped powders for both heat treatment temperatures.

Phase structure may be considered to be the main reason for obtaining higher surface reactivities with undoped NP powder heat treated at 600 °C and undoped AP powder heat treated at 700 °C. XRD analyses indicated that these powders have higher crystallite sizes and rutile weight fractions compared to the other powders. A well developed crystalline structure and a certain nanophase composition may be very important for the separation of charge carriers and light absorption. Undoped AP powder heat treated at 700 °C does not have blue and green light absorption bands, however the light absorption capacity may have increased due to the presence of rutile at a higher weight fraction compared to the other powders.

Another possible reason may be the increased electron-hole separation rates by the anatase-rutile junctions defined by the phase structure or TiO$_2$-Nd junctions for the doped powders. Anatase-rutile ratio is crucial in photocatalysis since anatase was reported to be more active and rutile has lower band gap than that of anatase.

CO/H$_2$ ratio is also an important parameter in the photocatalytic production of hydrogen. CO is formed by the decomposition of formic acid derived from methanol which may poison the catalyst and decrease the photocatalytic activity, hence minimum amount of CO production is desired for obtaining high hydrogen production with low impurity [54]. The highest CO/H$_2$ ratios were obtained with the powders possessing the highest H$_2$ production activities. The presence of lower anatase content in these powders may have decreased the oxidation rate of CO to CO$_2$.

The obtained high CO/H$_2$ ratios with the powders possessing the highest H$_2$ production activities may limit their use in the photocatalytic water splitting applications since producing high purity H$_2$ may be more important than
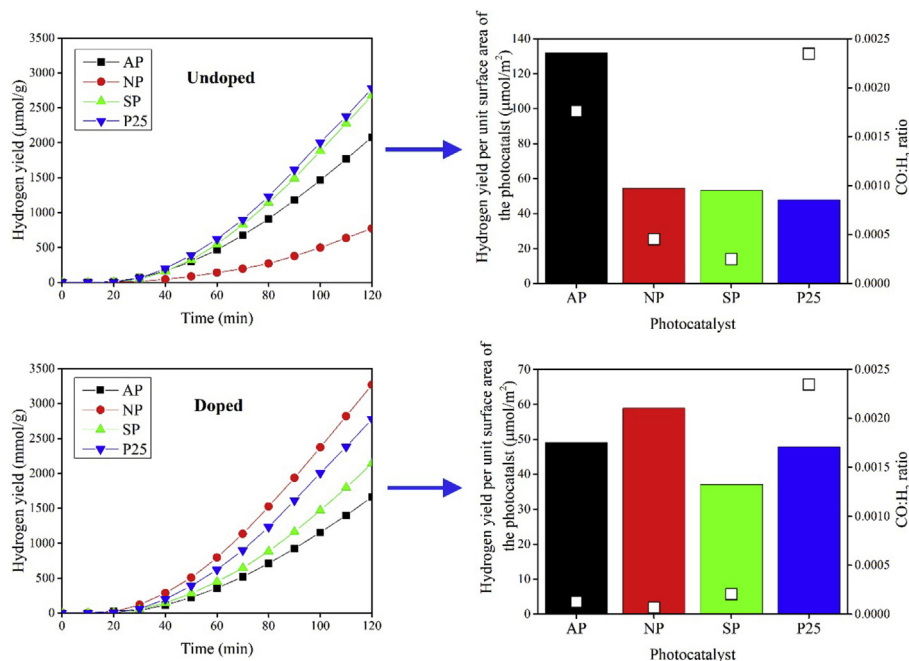
Fig. 9 — Time dependent hydrogen production (the left figure), hydrogen yields per unit surface area of the photocatalyst and CO:H_2 (□) ratios obtained at the end of 120 min (the right figure) with undoped/doped photocatalysts heat treated at 700 °C.

producing H_2 in higher quantities. Separation costs may be crucial. An optimum H_2 production rate with low CO/H_2 ratio is favourable as a design criterion in the production of sustainable and clean energy. In this respect using doped NP powders heat treated at 600° or 700 °C towards photocatalytic water splitting may be considered to be more reasonable for sustaining clean and cost effective energy production.
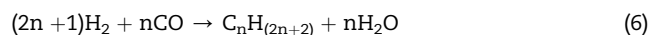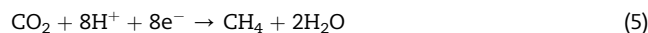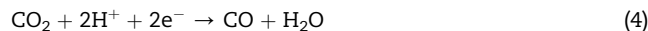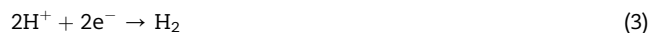
Photocatalytic CO_2 reduction

Photocatalytic reduction of CO_2 in the presence of water was conducted by using the same photocatalysts used in photocatalytic water splitting experiments without using Cu as co-catalyst. The gaseous products were tracked and CO was determined to be the main product of the photocatalytic CO_2 reduction experiments. Trace amounts of CH_4 and H_2 (which were out of our TCD quantification limits) evolution was also determined with the prepared powders. Photocatalytic CO_2 reduction activities of undoped/doped TiO_2 powders heat treated at 600 °C and 700 °C are given in Figs. 10 and 11, respectively.

CO yields were found to be the highest for undoped/doped NP powders heat treated at both temperatures. The surface reactivities should be compared here in order to have proper understanding while investigating the effects of phase structure and composition on the photocatalytic CO_2 reduction.

CO yields per unit surface area were found to be the highest for AP powders heat treated at 600 °C and NP powders heat treated at 700 °C. It was found that the produced CO amounts generally decreased with Nd doping in per unit area basis and increased in per amount of the powder basis. The increase in the surface area with Nd doping may be the main reason for the increased CO production amounts. At pH 7 (0.1 M NaOH purged with CO_2) the dissolution products of CO_2 are ~80% HCO_3^- and ~20% CO_2. The interaction of HCO_3^- with TiO_2

surface may have increased with Nd doping due to the surface area increase. CH_4 and H_2 evolution was also determined with the prepared powders. This may indicate that independent reactions involving 2 electrons and 8 electrons forming CO (reaction 4) and CH_4 (reaction 5), respectively [5] are the main reactions involving C in the photocatalytic reduction of CO_2 unlike a Fisher-Tropsch mechanism (reaction 6) [55]. The limited solubility of CO and H_2 molecules in water may restrain the further reduction to form molecules with higher carbon numbers, thus CO, CH_4 and H_2 leave the aqueous media and accumulate in the head space of the reactor.

$$TiO_2 + h\nu \rightarrow \tfrac{1}{2}\,O_2 + H^+ + e^- \tag{1}$$

$$CO_2 + e^- \rightarrow CO_2^- \tag{2}$$

$$2H^+ + 2e^- \rightarrow H_2 \tag{3}$$

$$CO_2 + 2H^+ + 2e^- \rightarrow CO + H_2O \tag{4}$$

$$CO_2 + 8H^+ + 8e^- \rightarrow CH_4 + 2H_2O \tag{5}$$

$$(2n+1)H_2 + nCO \rightarrow C_nH_{(2n+2)} + nH_2O \tag{6}$$

Probable reaction pathways for CO_2 photoreduction with undoped/doped TiO_2 powders are schematically shown in Fig. 12. Simultaneous multi-electronic processes may occur during the photocatalytic reduction of CO_2 according to the proposed mechanism. Electron-hole pairs are generated when TiO_2 is excited with the wavelengths no less than its band gap energy. A hole generated on the valence band react with water adsorbed on the surface of TiO_2 to produce ·OH, H^+ and O_2. The interaction of H^+ ion with the excited electron results in
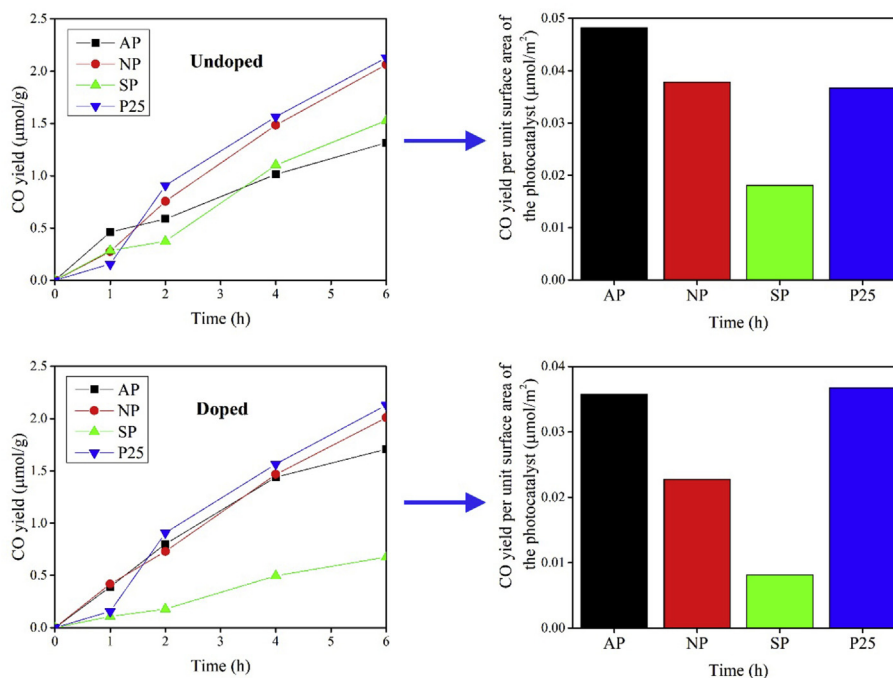
Fig. 10 — Time dependent CO production (the left figure) and CO yields per unit surface area of the photocatalyst obtained at the end of 120 min (the right figure) with undoped/doped photocatalysts heat treated at 600 °C.

Fig. 11 — Time dependent CO production (the left figure) and CO yields per unit surface area of the photocatalyst obtained at the end of 120 min (the right figure) with undoped/doped photocatalysts heat treated at 700 °C.
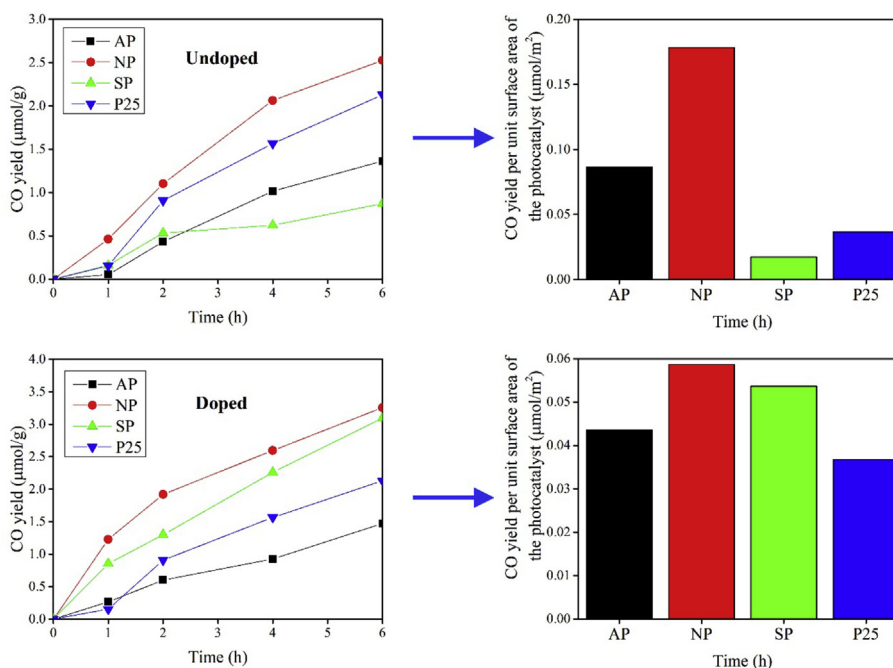
the formation of H· radical. Union of two H· radicals generates one H_2 molecule. On the conduction band, generated electron interacts with CO_2 and HCO_3^- to form $\cdot CO_2^-$ radical and HCO_3^-, respectively [56–58]. The formed H· radical reacts with $\cdot CO_2^-$ radical to form CO. CO is later reduced by one electron to form $\cdot CO^-$. Reaction of H· radical with $\cdot CO^-$ radical yields $\cdot C$ radical and OH^-. Consecutive reactions involving H· and $\cdot C$ radicals yield $\cdot CH_3$ radical. Finally, CH_4 (methane) or CH_3OH (methanol) molecules are formed when $\cdot CH_3$ radical reacts with H· radical or OH^-, respectively. Similar probable reaction pathways were also suggested elsewhere [59–61].
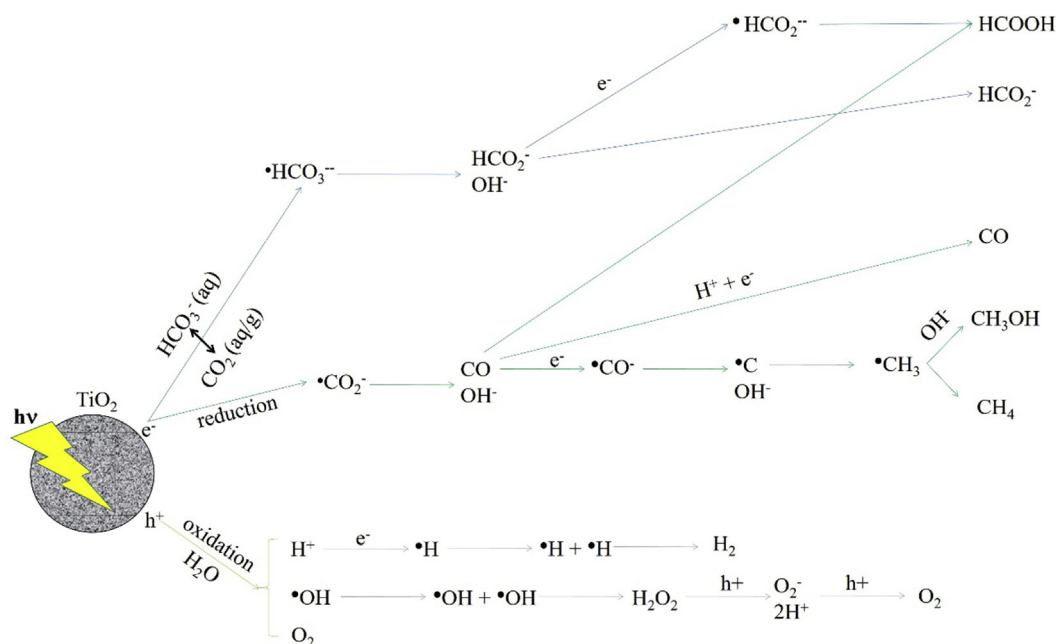
Fig. 12 — Probable reaction pathways for CO_2 photoreduction with undoped/doped TiO_2 powders prepared with different chemical routes.

Conclusions

In this study photocatalytic water splitting and CO_2 reduction activities of undoped and Nd doped TiO_2 powders prepared by different chemical routes were evaluated.

XRD, UV—Vis DRS and XPS analyses were conducted in order to develop a correlation between the photocatalytic activity and the powder properties altered by Nd doping and the preparation method employed. N and S doping in the TiO_2 lattice was induced by using excess amounts HNO_3 and H_2SO_4 in the powder preparation media.

The highest photocatalytic water splitting activity was obtained with undoped NP powder heat treated at 600 °C and doped NP powder heat treated at 700 °C. An optimum H_2 production rate with low CO/H_2 ratio is considered to be more favourable as a design criterion in the production of sustainable and clean energy. In this respect using doped NP powders heat treated at 600 °C or 700 °C towards photocatalytic water splitting is considered to be more reasonable for sustaining clean and cost effective energy production.

CO was determined to be the main product of the photocatalytic CO_2 reduction experiments. CO production was found to be the highest for undoped/doped NP powders heat treated at 600 °C and 700 °C, respectively. It was found that the produced CO amounts generally decreased with Nd doping on per unit area basis and increased in per amount of the powder. The increased CO production amounts was attributed to the increase in the surface area with Nd doping.

Artificial photosynthesis experiments indicated that photocatalytic activity may significantly depend on the nanophase structure of the photocatalyst. These findings revealed that high photocatalytic activities can be achieved by an optimization in the nanophase structure and electronic properties which can probably be designed by the employed powder preparation method.

Acknowledgements

REFERENCES

[1] Fujishima A, Honda K. Electrochemical photolysis of water at a semiconductor electrode. Nature 1972;238:37—8.
[2] Inoue T, Fujishima A, Konishi S, Honda K. Photoelectrocatalytic reduction of carbon dioxide in aqueous suspensions of semiconductor powders. Nature 1979;277:637—8.
[3] Yang Y, Ajmal S, Zheng X, Zhang L. Efficient nanomaterials for harvesting clean fuels from electrochemical and photoelectrochemical CO_2 reduction. Sustain Energy Fuels 2018;2:510—37.
[4] Chen Y, Wang D, Deng X, Li Z. Metal—organic frameworks (MOFs) for photocatalytic CO_2 reduction. Catalysis Sci Technol 2017;7:4893—904.
[5] Tahir M, Amin NS. Advances in visible light responsive titanium oxide-based photocatalysts for CO_2 conversion to hydrocarbon fuels. Energy Convers Manag 2013;76:194—214.
[6] Tahir M, Amin NS. Indium-doped TiO_2 nanoparticles for photocatalytic CO_2 reduction with H_2O vapors to CH_4. Appl Catal B Environ 2015;162:98—109.
[7] Zhao C, Krall A, Zhao H, Zhang Q, Li Y. Ultrasonic spray pyrolysis synthesis of Ag/TiO_2 nanocomposite photocatalysts for simultaneous H_2 production and CO_2 reduction. Int J Hydrogen Energy 2012;37:9967—76.

[8] Ahmad Beigi A, Fatemi S, Salehi Z. Synthesis of nanocomposite CdS/TiO$_2$ and investigation of its photocatalytic activity for CO$_2$ reduction to CO and CH$_4$ under visible light irradiation. J CO$_2$ Util 2014;7:23–9.

[9] Wang Q, An N, Bai Y, Hang H, Li J, Lu X, et al. High photocatalytic hydrogen production from methanol aqueous solution using the photocatalysts CuS/TiO$_2$. Int J Hydrogen Energy 2013;38:10739–45.

[10] Wang Q, Yun G, Bai Y, An N, Chen Y, Wang R, et al. CuS, NiS as co-catalyst for enhanced photocatalytic hydrogen evolution over TiO$_2$. Int J Hydrogen Energy 2014;39:13421–8.

[11] Qin G, Zhang Y, Ke X, Tong X, Sun Z, Liang M, et al. Photocatalytic reduction of carbon dioxide to formic acid, formaldehyde, and methanol using dye-sensitized TiO$_2$ film. Appl Catal B Environ 2013;129:599–605.

[12] Tseng IH, Wu JCS, Chou H-Y. Effects of sol–gel procedures on the photocatalysis of Cu/TiO$_2$ in CO$_2$ photoreduction. J Catal 2004;221:432–40.

[13] Ong W-J, Gui MM, Chai S-P, Mohamed AR. Direct growth of carbon nanotubes on Ni/TiO$_2$ as next generation catalysts for photoreduction of CO$_2$ to methane by water under visible light irradiation. RSC Adv 2013;3:4505–9.

[14] Menéndez-Flores VM, Nakamura M, Kida T, Jin Z, Murakami N, Ohno T. Controlled structure of anatase TiO$_2$ nanoparticles by using organic additives in a microwave process. Appl Catal Gen 2011;406:119–23.

[15] Wang Q, Lian J, Bai Y, Hui J, Zhong J, Li J, et al. Photocatalytic activity of hydrogen production from water over TiO$_2$ with different crystal structures. Mater Sci Semicond Process 2015;40:418–23.

[16] Ni M, Leung MKH, Leung DYC, Sumathy K. A review and recent developments in photocatalytic water-splitting using for hydrogen production. Renew Sustain Energy Rev 2007;11:401–25.

[17] Ola O, Maroto-Valer MM. Review of material design and reactor engineering on TiO$_2$ photocatalysis for CO$_2$ reduction. J Photochem Photobiol C Photochem Rev 2015;24:16–42.

[18] Bellardita M, Addamo M, Di Paola A, Palmisano L. Photocatalytic behaviour of metal-loaded TiO$_2$ aqueous dispersions and films. Chem Phys 2007;339:94–103.

[19] Bellardita M, Di Paola A, Palmisano L, Parrino F, Buscarino G, Amadelli R. Preparation and photoactivity of samarium loaded anatase, brookite and rutile catalysts. Appl Catal B Environ 2011;104:291–9.

[20] Chiou C-H, Juang R-S. Photocatalytic degradation of phenol in aqueous solutions by Pr-doped TiO$_2$ nanoparticles. J Hazard Mater 2007;149:1–7.

[21] Hassan MS, Amna T, Yang OB, Kim H-C, Khil M-S. TiO$_2$ nanofibers doped with rare earth elements and their photocatalytic activity. Ceram Int 2012;38:5925–30.

[22] Jian Z, Pu Y, Fang J, Ye Z. Microemulsion synthesis of nanosized TiO$_2$ particles doping with rare-earth and their photocatalytic activity. Photochem Photobiol 2010;86:1016–21.

[23] Reszczyńska J, Grzyb T, Sobczak JW, Lisowski W, Gazda M, Ohtani B, et al. Lanthanide co-doped TiO$_2$: the effect of metal type and amount on surface properties and photocatalytic activity. Appl Surf Sci 2014;307:333–45.

[24] Cruz Romero D, Torres GT, Arévalo JC, Gomez R, Aguilar-Elguezabal A. Synthesis and characterization of TiO$_2$ doping with rare earths by sol–gel method: photocatalytic activity for phenol degradation. J Sol Gel Sci Technol 2010;56:219–26.

[25] Tong T, Zhang J, Tian B, Chen F, He D, Anpo M. Preparation of Ce–TiO$_2$ catalysts by controlled hydrolysis of titanium alkoxide based on esterification reaction and study on its photocatalytic activity. J Colloid Interface Sci 2007;315:382–8.

[26] Wang C, Ao Y, Wang P, Hou J, Qian J. Preparation, characterization and photocatalytic activity of the neodymium-doped TiO$_2$ hollow spheres. Appl Surf Sci 2010;257:227–31.

[27] Xie Y, Yuan C. Characterization and photocatalysis of Eu^{3+}–TiO$_2$ sol in the hydrosol reaction system. Mater Res Bull 2004;39:533–43.

[28] Xu Y-H, Chen C, Yang X-L, Li X, Wang B-F. Preparation, characterization and photocatalytic activity of the neodymium-doped TiO$_2$ nanotubes. Appl Surf Sci 2009;255:8624–8.

[29] Asal S, Saif M, Hafez H, Mozia S, Heciak A, Moszyński D, et al. Photocatalytic generation of useful hydrocarbons and hydrogen from acetic acid in the presence of lanthanide modified TiO$_2$. Int J Hydrogen Energy 2011;36:6529–37.

[30] Puskelova J, Michal R, Caplovicova M, Antoniadou M, Caplovic L, Plesch G, et al. Hydrogen production by photocatalytic ethanol reforming using Eu- and S-doped anatase. Appl Surf Sci 2014;305:665–9.

[31] Zalas M, Laniecki M. Photocatalytic hydrogen generation over lanthanides-doped titania. Sol Energy Mater Sol Cell 2005;89:287–96.

[32] Zhang J, Yan S, Zhao S, Xu Q, Li C. Photocatalytic activity for H$_2$ evolution of TiO$_2$ with tuned surface crystalline phase. Appl Surf Sci 2013;280:304–11.

[33] Tian M, Wang H, Sun D, Peng W, Tao W. Visible light driven nanocrystal anatase TiO$_2$ doped by Ce from sol–gel method and its photoelectrochemical water splitting properties. Int J Hydrogen Energy 2014;39:13448–53.

[34] Liu Y, Zhou S, Li J, Wang Y, Jiang G, Zhao Z, et al. Photocatalytic reduction of CO$_2$ with water vapor on surface La-modified TiO$_2$ nanoparticles with enhanced CH$_4$ selectivity. Appl Catal B Environ 2015;168–169:125–31.

[35] Matějová L, Kočí K, Reli M, Čapek L, Hospodková A, Peikertová P, et al. Preparation, characterization and photocatalytic properties of cerium doped TiO$_2$: on the effect of Ce loading on the photocatalytic reduction of carbon dioxide. Appl Catal B Environ 2014;152–153:172–83.

[36] Ogura K, Kawano M, Yano J, Sakata Y. Visible-light-assisted decomposition of H$_2$O and photomethanation of CO$_2$ over CeO$_2$-TiO$_2$ catalyst. J Photochem Photobiol Chem 1992;66:91–7.

[37] Wang Y, Li B, Zhang C, Cui L, Kang S, Li X, et al. Ordered mesoporous CeO$_2$-TiO$_2$ composites: highly efficient photocatalysts for the reduction of CO$_2$ with H$_2$O under simulated solar irradiation. Appl Catal B Environ 2013;130–131:277–84.

[38] Zhao C, Liu L, Zhang Q, Wang J, Li Y. Photocatalytic conversion of CO$_2$ and H$_2$O to fuels by nanostructured Ce-TiO$_2$/SBA-15 composites. Catal Sci Technol 2012;2:2558–68.

[39] Sun Z, Hu Z, Yan Y, Zheng S. Effect of preparation conditions on the characteristics and photocatalytic activity of TiO$_2$/purified diatomite composite photocatalysts. Appl Surf Sci 2014;314:251–9.

[40] Spurr RA, Myers H. Quantitative analysis of anatase-rutile mixtures with an X-ray diffractometer. Anal Chem 1957;29:760–2.

[41] Tripathi AK, Singh MK, Mathpal MC, Mishra SK, Agarwal A. Study of structural transformation in TiO$_2$ nanoparticles and its optical properties. J Alloy Comp 2013;549:114–20.

[42] Kruse N, Chenakin S. XPS characterization of Au/TiO$_2$ catalysts: binding energy assessment and irradiation effects. Appl Catal Gen 2011;391:367–76.

[43] Wagner CD, Davis LE, Zeller MV, Taylor JA, Raymond RH, Gale LH. Empirical atomic sensitivity factors for quantitative analysis by electron spectroscopy for chemical analysis. Surf Interface Anal 1981;3:211–25.

[44] López R, Gómez R. Band-gap energy estimation from diffuse reflectance measurements on sol—gel and commercial TiO$_2$: a comparative study. J Sol Gel Sci Technol 2012;61:1—7.

[45] Swamy V, Menzies D, Muddle BC, Kuznetsov A, Dubrovinsky LS, Dai Q, et al. Nonlinear size dependence of anatase TiO$_2$ lattice parameters. Appl Phys Lett 2006;88:243103.

[46] Yang G, Jiang Z, Shi H, Xiao T, Yan Z. Preparation of highly visible-light active N-doped TiO$_2$ photocatalyst. J Mater Chem 2010;20:5301—9.

[47] Yu JC, Ho W, Yu J, Yip H, Wong PK, Zhao J. Efficient visible-light-induced photocatalytic disinfection on sulfur-doped nanocrystalline titania. ES T (Environ Sci Technol) 2005;39:1175—9.

[48] Maurya A, Chauhan P, Mishra SK, Srivastava RK. Structural, optical and charge transport study of rutile TiO$_2$ nanocrystals at two calcination temperatures. J Alloy Comp 2011;509:8433—40.

[49] Sun B, Zhou G, Shao C, Jiang B, Pang J, Zhang Y. Spherical mesoporous TiO$_2$ fabricated by sodium dodecyl sulfate-assisted hydrothermal treatment and its photocatalytic decomposition of papermaking wastewater. Powder Technol 2014;256:118—25.

[50] Di Valentin C, Finazzi E, Pacchioni G, Selloni A, Livraghi S, Paganini MC, et al. N-doped TiO$_2$: theory and experiment. Chem Phys 2007;339:44—56.

[51] Nishikiori H, Hayashibe M, Fujii T. Visible light-photocatalytic activity of sulfate-doped titanium dioxide prepared by the Sol—Gel method. Catalysts 2013;3:363.

[52] Yan G, Zhang M, Hou J, Yang J. Photoelectrochemical and photocatalytic properties of N + S co-doped TiO$_2$ nanotube array films under visible light irradiation. Mater Chem Phys 2011;129:553—7.

[53] Peng F, Cai L, Yu H, Wang H, Yang J. Synthesis and characterization of substitutional and interstitial nitrogen-doped titanium dioxides with visible light photocatalytic activity. J Solid State Chem 2008;181:130—6.

[54] Wu G, Chen T, Su W, Zhou G, Zong X, Lei Z, et al. H$_2$ production with ultra-low CO selectivity via photocatalytic reforming of methanol on Au/TiO$_2$ catalyst. Int J Hydrogen Energy 2008;33:1243—51.

[55] Hoffmann MR, Moss JA, Baum MM. Artificial photosynthesis: semiconductor photocatalytic fixation of CO$_2$ to afford higher organic compounds. Dalton Trans 2011;40:5151—8.

[56] Hussain M, Akhter P, Saracco G, Russo N. Nanostructured TiO$_2$/KIT-6 catalysts for improved photocatalytic reduction of CO$_2$ to tunable energy products. Appl Catal B Environ 2015;170—171:53—65.

[57] Sreekanth N, Phani KL. Selective reduction of CO$_2$ to formate through bicarbonate reduction on metal electrodes: new insights gained from SG/TC mode of SECM. Chem Commun 2014;50:11143—6.

[58] Zhang Q, Lin C-F, Chen B-Y, Ouyang T, Chang C-T. Deciphering visible light photoreductive conversion of CO$_2$ to formic acid and methanol using waste prepared material. Environ Sci Technol 2015;49:2405—17.

[59] Liu L, Zhao H, Andino JM, Li Y. Photocatalytic CO$_2$ reduction with H$_2$O on TiO$_2$ nanocrystals: comparison of anatase, rutile, and brookite polymorphs and exploration of surface chemistry. ACS Catal 2012;2:1817—28.

[60] Kim J, Do JY, Park N-K, Lee SJ, Hong J-P, Kang M. Photoreduction of CO$_2$ into CH$_4$ using Bi$_2$S$_3$-TiO$_2$ double-layered dense films. Kor J Chem Eng 2018;35:1089—98.

[61] Zhang Q, Liu F, Hong JM, Lin C-F, Chang C-T. Efficiency, mechanism and kinetics research of CO$_2$ photo reduction by graphene-TiO$_2$ under visible light. J Nanosci Nanotechnol 2017;17:5073—80.